HHS Public Access

Author manuscript

Optica. Author manuscript; available in PMC 2025 January 25.

Published in final edited form as:

Optica. 2021 June 20; 8(6): 885–897. doi:10.1364/optica.426870.

Instant FLIM enables 4D *in vivo* lifetime imaging of intact and injured zebrafish and mouse brains

Yide Zhang[1,6], **Ian H. Guldner**[2,4,5], **Evan L. Nichols**[2,3], **David Benirschke**[1], **Cody J. Smith**[2,3], **Siyuan Zhang**[2,4,5], **Scott S. Howard**[1,4,*]

[1]Department of Electrical Engineering, University of Notre Dame, Notre Dame, IN 46556, USA

[2]Department of Biological Sciences, University of Notre Dame, Notre Dame, IN 46556, USA

[3]Center for Stem Cells and Regenerative Medicine, University of Notre Dame, IN 46556, USA

[4]Mike and Josie Harper Cancer Research Institute, University of Notre Dame, IN 46556, USA

[5]Indiana University Melvin and Bren Simon Cancer Center, Indianapolis, IN 46202, USA

[6]Caltech Optical Imaging Laboratory, Andrew and Peggy Cherng Department of Medical Engineering, Department of Electrical Engineering, California Institute of Technology, Pasadena, CA 91125, USA

Abstract

Traditional fluorescence microscopy is blind to molecular microenvironment information that is present in fluorescence lifetime, which can be measured by fluorescence lifetime imaging microscopy (FLIM). However, most existing FLIM techniques are slow to acquire and process lifetime images, difficult to implement, and expensive. Here, we present instant FLIM, an analog signal processing method that allows real-time streaming of fluorescence intensity, lifetime, and phasor imaging data through simultaneous image acquisition and instantaneous data processing. Instant FLIM can be easily implemented by upgrading an existing two-photon microscope using cost-effective components and our open-source software. We further improve the functionality, penetration depth, and resolution of instant FLIM using phasor segmentation, adaptive optics, and super-resolution techniques. We demonstrate through-skull intravital 3D FLIM of mouse brains to depths of 300 μm and present the first *in vivo* 4D FLIM of microglial dynamics in intact and injured zebrafish and mouse brains up to 12 hours.

1. Introduction

Imaging molecular contrast is essential to continued advances in cellular biology. Fluorescence microscopy has been a significant tool over the past decades in imaging cellular and sub-cellular molecular contrast [1]. Traditional fluorescence microscopy typically obtains molecular contrast by labeling parts of cells with different fluorophores and imaging emission intensity. However, fluorescence emission contains a wealth of

* showard@nd.edu .

Disclosures. The authors declare that there are no competing interests.

Supplemental document. See Supplement 1 for supporting content.

information on the molecular microenvironment that is not captured by the emission intensity but is present in the fluorescence lifetime. By performing fluorescence lifetime imaging microscopy (FLIM), fluorophores with overlapping emission spectra can be differentiated as long as their lifetimes are different, and physiological parameters such as pH, refractive index, ion concentration, dissolved gas concentration, and Förster resonance energy transfer (FRET) can be measured [2–5]. When combined with multiphoton microscopy (MPM) [6,7], FLIM can provide lifetime measurements *in vivo* with high resolution, deep penetration, and reduced photodamage [8,9]. Despite the biologically-relevant information provided by fluorescence lifetime, the widespread use of FLIM in biomedical imaging has been limited due to its slow image acquisition and processing speed, low signal-to-noise ratio (SNR), difficult implementation, and high instrumentation cost [10–17].

State-of-the-art time-domain (TD) [15,16,18–23] and frequency-domain (FD) [11,13,24–27] FLIM techniques have been developed to overcome the limitations above. The most widely used and commercialized TD-FLIM technique is time-correlated single-photon counting (TCSPC), which extracts the lifetime information from a histogram acquired by repetitively recording the arrival time of each photon [18–20,22]. Whereas state-of-the-art TCSPC systems can acquire fluorescence decay data at around 10 μs/pixel, they cannot generate lifetime images immediately using a regular computer due to the complicated post-processing procedures (e.g., deconvolution and curve-fitting) applied to the time-resolved fluorescence data acquired at GB/s rates [16]. Therefore, most TCSPC systems store the raw data to the hard drive during the imaging session, and then post-process the data offline to get lifetime results. Without GPU processing, the data processing time for large TCSPC images (e.g., 1-Megapixel) are several minutes [28]; GPU processing can reduce the time to a few seconds, which, however, still cannot satisfy the real-time requirement. To reduce the data processing time, Ryu et al. employed the analog mean-delay (AMD) method to extract the TD lifetime information through numerical integration and realized real-time visualization of fixed tissues [15]. Li et al. developed a center-of-mass method (CMM) to implement real-time TD lifetime calculations in hardware [29–31]. Besides TCSPC, Bower et al. utilized a high-frequency digitizer to directly sample the TD fluorescence signal and achieved high-speed imaging of metabolic dynamics in living cells [16]. While both the AMD and the direct sampling methods reduced the pixel dwell time to below 10 μs, they required expensive high-frequency digitizers (>$10,000), and the limited computer memory and bandwidth prevented them from streaming lifetime images without interruption due to the large amount of data sampled by the digitizers [16]. On the other hand, FD-FLIM techniques are less commonly used or commercialized compared to TD-FLIM approaches due to their relatively difficult implementation and low SNR in lifetime measurements [10,14]. Conventional FD-FLIM techniques typically require external modulation sources (usually sinusoidal modulation), high-voltage but imperfect (less than 100% modulation degree) detector gain modulation, sequential phase shifting, specialized electronics, and can achieve lifetime image acquisition and processing as fast as 40 μs/pixel [11,13,24,26,32,33]. Recently, Raspe et al. demonstrated siFLIM, an FD-FLIM technique capable of video-rate (around 10 frames per second) lifetime imaging of living cells [27]. However, siFLIM requires a dedicated camera, and it relies on a widefield microscope with

no optical sectioning capabilities; therefore, it cannot be used to acquire 3D lifetime images. Overall, due to the limitations in acquisition or processing speed, SNR, or optical sectioning capabilities, so far, only a few existing FLIM systems have demonstrated 3D lifetime imaging; no systems, however, have demonstrated long-term, time-lapse 3D (i.e., 4D) *in vivo* FLIM through-skull deep in the brain, where useful ballistic photons are scarce due to severe scattering, and prolonged imaging time is not feasible because of animal movements [34]. Moreover, for functional imaging experiments *in vivo* where animals under anesthesia have limited experimental time, operators typically want the experiment to progress based on the real-time outcomes of lifetime measurements; this would not be possible without an *in vivo* FLIM system that can generate lifetime outcomes instantaneously, a requirement that cannot be satisfied with existing FLIM techniques.

Here, we demonstrate instant FLIM, a novel FD-FLIM technique that utilizes analog signal processing to simultaneously address the challenges in image acquisition and processing, SNR, implementation, and cost faced by existing FLIM methods. We present instant FLIM as a tool that provides real-time streaming of two-photon fluorescence intensity, lifetime, and phasor imaging data through basic matrix operations applied to the analog data acquired at MB/s rates, as well as the first FLIM technique that allows instantaneous generation of lifetime measurements for functional imaging experiments *in vivo*. The word "instant" refers to acquiring FLIM data simultaneously with instantaneous processing, where lifetime images and phasor plots [35,36] are instantaneously generated without recording the fluorescence decay curves, thus eliminating the limitations not only in the speed but also the computer memory and bandwidth faced by state-of-the-art FLIM techniques [15,16]. We show that an instant FLIM system can be easily implemented as an upgrade to an existing two-photon laser scanning microscope for under $2,500 using cost-effective off-the-shelf components and our open-source, highly modularized, and user-friendly software packages. We also show that the imaging functionality, penetration depth, and resolution of an instant FLIM system can be further improved using phasor segmentation [37], adaptive optics [38], and super-resolution FLIM [39–41] techniques. Finally, employing an instant FLIM system, we demonstrate intravital 3D lifetime imaging of mouse brains through-skull to depths of 300 μm, and present the first long-term, *in vivo* 4D lifetime imaging of microglial dynamics in intact and injured larval zebrafish and adult mouse brains up to 12 hours.

2. Materials and Methods

2.1 Experimental setup and analog signal processing

We implemented the instant FLIM system based on a custom-built two-photon laser scanning microscope (Fig. 1A; Fig. S1). The intensity of a mode-locked Ti:sapphire laser (Spectra-Physics Mai Tai BB, 710–990 nm, 100 fs, 80 MHz) is controlled by a neutral density filter (NDF), a motorized half-wave plate, and a polarizing beam splitter (PBS). A power meter is used to measure the excitation power by monitoring a small fraction of the laser beam reflected by a glass slide. A mechanical shutter (Thorlabs SHB1T) is used to block the laser beam when no imaging acquisition takes place. A sensorless adaptive optics (AO) setup consisting of a deformable mirror (Thorlabs DMP40-P01), a beam expander composed of two achromatic doublets (Thorlabs AC254–030-B, AC254–075-B),

an achromatic quarter-wave plate (Thorlabs AQWP05M-980), and another PBS is utilized to correct the wavefront of the excitation beam in order to improve the imaging depth (Section S4). The AO setup is optional and can be switched into and out of the optical path using a folding mirror. The laser beam is directed to a conventional two-photon microscopy setup consisting of a pair of galvo scanners (Thorlabs GVS002), a scan lens (Thorlabs AC254–040-B), a tube lens (Thorlabs AC254–200-B), an objective lens (Nikon CFI APO NIR, 40x, 0.8 NA, or Olympus XLPLN25XWMP2, 25x, 1.05 NA), and a motorized stage (Prior OptiScan III). A long pass filter is used to block ambient light from entering the objective. The 2PEF is epi-collected by the objective lens, reflected by a dichroic mirror, filtered through a set of bandpass and short pass filters to eliminate residual excitation, and detected by a photomultiplier tube (PMT) (Hamamatsu H7422PA-40) through a collection lens.

The analog signal processing module in instant FLIM utilizes the fluorescence signal from the PMT and the 80 MHz reference signal from the Ti:sapphire laser to generate the intensity, lifetime, and phasor data simultaneously. As shown in Fig. S2, the current signal from the PMT is amplified and converted to a voltage signal by a transimpedance amplifier (Aricorp DC-100), filtered by a low pass filter (LPF) (Mini-Circuits BLP-90+), and separated into DC and RF parts by a bias tee (Mini-Circuits ZFBT-282–1.5A+). The DC signal (V_{DC}) is acquired by a data acquisition (DAQ) card (National Instruments PCIe-6323) to reconstruct the intensity image. The RF signal is amplified by a low-noise amplifier (LNA) (Mini-Circuits ZX60-P103LN+) and split to four paths by a 4-way power splitter (Mini-Circuits ZSC-4–3+). Meanwhile, the 80 MHz reference signal from the laser, $\upsilon_{ref}(t)$, is filtered by an LPF to eliminate higher harmonics, amplified by an LNA, and split to four signal paths, $\upsilon_{80MHz}(t)$, also by a power splitter. A phase shift is introduced to each reference signal path by a pair of phase shifters (Mini-Circuits JSPHS-150 with TB-152+). Note that each phase shifter can introduce a phase shift within π to the 80 MHz signal; connecting them in tandem introduces a total phase shift within 2π for each path. The phase shifts are independently controlled by the bias voltages generated by the DAQ card. The four phase-shifted reference signals are then amplified by LNAs and directed to four RF mixers (Mini-Circuits ZAD-3H+). Each mixer takes a reference signal path, $\upsilon_{LO}(t, \varphi)$, to its local oscillator (LO) port and a PMT signal path, $\upsilon_{RF}(t)$, to its RF port and generates a mixed signal, $\upsilon_{IF}(t, \varphi)$, on its intermediate frequency (IF) port. The IF signals from each mixer are then filtered to DC, i.e., $V_{IF}(\varphi)$, by an LPF (Thorlabs EF502) and measured by another DAQ card (National Instruments PCI-6110). In the end, for each intensity image (2D, 3D, or 4D) acquired, four corresponding mixer images are acquired simultaneously, so the data acquisition is intrinsically synchronized and effect of the PMT timing jitter is minimized. Fluorescence lifetime images as well as phasor plots are then instantaneously generated through basic matrix operations. The DAQ cards are also used to control the motorized half-wave plate, the shutter, and the galvo scanners during the imaging process. The motorized stage and the deformable mirror, on the other hand, are controlled directly by the computer through universal serial bus (USB) ports. Note that all electronic components in the instant FLIM system are impedance matched to 50 Ω to suppress signal reflections, and LNAs are used and the RF components are properly shielded to minimize additional electronic noise introduced to the measurement.

The parts and price list for the implementation of an instant FLIM system is presented in Table S2. The total cost to upgrade an existing two-photon laser scanning microscope (including data acquisition devices) to an instant FLIM system is less than $2,500.

2.2 Simultaneous acquisition and processing of intensity, lifetime, and phasor data

With the analog signal processing in instant FLIM, the fluorescence intensity, lifetime, and phasor data can be acquired simultaneously (Fig. 1B; Section S1). Specifically, the 2PEF intensity image is generated from the DC part of the PMT signal:

$$V_{\mathrm{DC}} = \frac{BP^2c}{T} + O_B, \tag{1}$$

where P is the excitation power, c is the fluorophore concentration, T is the modulation period of the Ti:sapphire laser, B and O_B are the conversion loss and offset from the bias tee's RF&DC to DC ports, respectively. The lifetime and phasor data, on the other hand, are obtained by applying basic mathematical operations on the outputs of the four mixers' IF ports:

$$V_{\mathrm{IF}}(\varphi) = \frac{MP^2c}{T}\sum_i a_i \frac{1}{1+\tau_i\omega}[\sin(\varphi) + \tau_i\omega\cos(\varphi)] + O_M, \tag{2}$$

where φ is the phase shift introduced by the phase shifters, a_i is the intensity-weighted fractional contribution of the fluorophore with lifetime τ_i $(\sum_i a_i = 1)$, ω is the angular modulation frequency, M and O_M are the conversion loss and offset from the mixer's RF to IF ports, respectively. The average (phase) lifetime [2] image is calculated as

$$\tau = \frac{1}{\omega}\frac{V_{\mathrm{IF}}(0) - V_{\mathrm{IF}}(\pi)}{V_{\mathrm{IF}}(0.5\pi) - V_{\mathrm{IF}}(1.5\pi)}, \tag{3}$$

and the components of the phasors are obtained as

$$\begin{aligned} g &= \frac{B}{2M}\frac{V_{\mathrm{IF}}(0.5\pi) - V_{\mathrm{IF}}(1.5\pi)}{V_{\mathrm{DC}} - O_B} = \sum_i a_i \frac{1}{1+(\tau_i\omega)^2}, \\ s &= \frac{B}{2M}\frac{V_{\mathrm{IF}}(0) - V_{\mathrm{IF}}(\pi)}{V_{\mathrm{DC}} - O_B} = \sum_i a_i \frac{\tau_i\omega}{1+(\tau_i\omega)^2}, \end{aligned} \tag{4}$$

where M/B and O_B are calibrated before measurements using the procedures detailed in Section S2.

2.3 Image reconstruction and analysis

All image reconstructions and analyses were performed with our open-source *Instant-FLIM-Control* and *Instant-FLIM-Analysis* (Fig. S5) software developed for this work. Additional image processing and visualization were performed using ImageJ (US National Institutes of Health), Matlab (MathWorks), Imaris (Bitplane), or Illustrator (Adobe) software.

The raw intensity [Eq. (1)], g, and s [Eq. (4)] images from 2D, 3D, and 4D instant FLIM measurements were exported as 32-bit TIF files using the *Instant-FLIM-Control* program. Whereas the program allows the export of additional FLIM data, to reduce the consumption of the computer's storage space, we exported only the raw intensity, g, and s images, which can be used to reconstruct other types of FLIM data. We used the "Correct 3D Drift" ImageJ plugin [42] to register the 4D raw images to correct for the sample drift during time-lapse measurements. To perform the image registration simultaneously on the three raw images, we created a color image by merging the raw intensity, g, and s images as its red, green, and blue channels, respectively; then, as the 3D image registration was performed on the red (intensity) channel, the other channels were registered simultaneously. The registered image was cropped to remove the empty voxels generated from the registration process, and its channels were split into three separate images, which correspond to the registered intensity, g, and s images.

The intensity, g, and s images were then imported to the *Instant-FLIM-Analysis* program to generate other types of FLIM data. Since the raw FLIM data usually have a low SNR [14], we provided a filtering option in the program, such that one could apply a median filter (3×3 or 5×5 kernels) or a smoothing filter on the raw images, one or multiple times, to increase the SNR; note that applying a median filter to the phasor images does not decrease the image resolution [36]. In this work, we applied a 3×3 median filter three times on the raw phasor images for all *in vivo* measurements. The program could also uniformly scale the g and s images by a constant ratio to effectively zoom-in or zoom-out the phasor plot while keeping the calculated lifetime unaltered; a ratio between 0.7 to 1.0 was used in our measurements to post-compensate for the inaccuracy in system calibration and make sure that the majority of the phasor points fall inside the universal semicircle $[(g-0.5)^2+s^2=0.25]$. We then generated the phasor plot from the pre-processed g and s images. The phasor plot was a 2D histogram of the phasor components, g and s, where the magnitude (represented with a color map) of each grid (with a pre-defined size) in the 2D histogram represented the number of phasor points located inside that grid. Note that the phasor plot could be generated simultaneously with intensity and lifetime images in the *Instant-FLIM-Control* program. In the *Instant-FLIM-Analysis* program, however, the phasor plot could be further analyzed using phasor-based image segmentation techniques. To perform the phasor analysis, the program allowed the user to either (a) manually draw ROIs on the phasor plot and segment the pixels corresponding to the phasor points enclosed by the ROIs with different colors [36], or (b) automatically group the phasors into K clusters using the K-means clustering algorithm and segment the pixels corresponding to the phasor clusters with different colors [37]; both techniques could segment the raw image into structures with different lifetime/phasor characteristics (Fig. S6). After the analysis described above, the raw lifetime image (gray-scale image with pixel value as lifetime),

composite lifetime image (RGB image with pixel brightness as intensity, hue as lifetime), phasor plot (RGB image), and segmented images based on phasor labeling or phasor clustering techniques (RGB image) were generated and exported as 32-bit TIF files. For 3D images, the TIF files were imported into ImageJ and the maximized z-projections of the stacks were generated. For 4D measurements, the stacks were first converted to hyperstacks in ImageJ to facilitate the time-lapse analysis, and a time-lapse maximized z-projection sequence could be generated. We also used Imaris to visualize the 3D and 4D stacks and enhance the qualitative information of FLIM by surface rendering the composite lifetime images.

To quantify the results of *in vivo* instant FLIM measurements (Fig. 3-Fig. 6), we extracted the raw lifetime as well as g and s values from the TIF files exported by the *Instant-FLIM-Analysis* program. Specifically, the files were opened in ImageJ, a single-plane ROI was drawn around the cell of interest, and the mean value was measured within that ROI. The plots representing the phasor locations of cells were generated using Illustrator (Fig. 3D, Fig. 5C). Using the *Instant-FLIM-Analysis* program, ROIs were drawn on the phasor plots to correspond with the pixels representing individual cells. Individual ROIs were drawn for each cell analyzed. The locations for each of these ROIs were then recapitulated within the universal phasor semicircle. These specific locations were determined by exporting each phasor plot with the drawn ROIs and determining the coordinates of the ROIs within the exported phasor plot image using ImageJ. The coordinates were then used to place representations of each cell in the proper location within the universal phasor semicircle in Illustrator. In Fig. 3-Fig. 6 separate statistical tests on τ, g, and s were performed to directly compare lifetime measurements between experimental groups. This method allows for determination of specific lifetime components which are different between samples or experimental conditions.

2.4 Animal procedures and sample preparation

All animal studies were conducted in accordance with the University of Notre Dame Institutional Animal Care and Use Committee guidance. The acquisition parameters for all the images shown in this work are presented in Table S1. Note that the excitation power and pixel dwell time in each imaging experiment were controlled carefully to prevent photobleaching.

Intravital imaging of the mouse brain was performed similarly to previously described [43]. Briefly, Cx3cr1-GFP/+ mice (generated in-house by crossing Cx3cr1-GFP/GFP mice with wildtype C57Bl/6 mice) were anesthetized with ketamine and xylazine cocktail by intraperitoneal injection. The mouse's head was secured and fixed in place using a stereotaxic instrument (Stoelting Co), and the skull was exposed with a midline scalp incision. A high-speed microdrill (Ideal Microdrill) equipped with a 0.7 mm burr (Fine Science Tools, 19007–09) was used to thin the skull to approximately 30 μm in thickness, using light sweeping motions to thin the skull gradually without applying significant pressure to the brain. In some instances, dental cement was used to border the thinned skull to form a bowl-like barrier to help contain water for imaging. Following surgery, the anesthetized mouse was administered a retro-orbital injection of 70 kDa Texas Red-Dextran

(Invitrogen D1864) to enable fluorescent detection of blood vessels. The mouse was placed on the stage for imaging and its heart rate, respiration rate, and toe-pinch reflex were monitored periodically to ensure that it was fully anesthetized and not under duress.

The transgenic zebrafish line used in this study was *Tg(pu1:gfp)*. All embryos were generated from pairwise matings and raised at 28 °C until imaging. Stable, germline transgenic zebrafish were used for all experiments. Embryos of either sex were used for all experiments. At 4 dpf, the embryos were dechorionated and anesthetized with 3-amino-benzoic acid ester. After anesthetization, embryos were mounted on their ventral side in 0.8% low-melting-point agarose in 35 mm Petri dishes with glass bottoms. Following mounting, the embryos were imaged using the instant FLIM system described above.

To prepare a fixed mouse brain to image for select experiments, a living Cx3cr1-GFP/+ mouse was first deeply anesthetized with isoflurane. Next, the mouse's chest cavity was opened to expose the heart, and the mouse was provided with a 100 μL injection of fixable Dextran 594 directly into the heart. After allowing the dextran to circulate for 1 minute, the mouse was perfused with 10 mL ice-cold 4% PFA to thoroughly fix the brain. Subsequently, the brain was extracted and fixed in 4% PFA overnight at 4 °C, and washed in 1x PBS, after which point it was ready for imaging.

MDA-MB-231-EGFP cells were cultured in DMEM High Glucose supplemented with 10% FBS and 1% Penicillin-Streptomycin in an incubator at 37 °C, 5% CO_2. Prior to imaging, the cells were grown to about 80% confluence for the imaging experiments. During imaging, refrigerated or heated culture media were added to the cell culture to change the microenvironment temperature, which was simultaneously monitored by a thermometer placed in the media.

FluoCells prepared slide #1 (Invitrogen F36924) was used as a biological test slide to evaluate the performance of the instant FLIM system. This test slide contained bovine pulmonary artery endothelial (BPAE) cells labeled with multiple fluorescent dyes: the mitochondria were stained with MitoTracker Red CMXRos, the F-actin was labeled with Alexa Fluor 488 phalloidin, and the nuclei were labeled with DAPI.

Four lifetime standards, i.e., fluorophore solutions with known fluorescence lifetimes, were prepared as previously described [44,45]: 1 mM coumarin 6 in methanol (2.3 ns at 20 °C), 1 mM coumarin 6 in ethanol (2.4 ns at 20 °C), 1mM fluorescein in 0.1 M NaOH (4.0 ns at 20 °C), and 1 mM rhodamine B in water (1.7 ns at 20 °C). To prepare the standards, the coumarin 6 (Sigma-Aldrich 546283) was dissolved in methanol (VWR BDH2029) and ethanol (Millipore 818760), respectively; the fluorescein (Sigma-Aldrich F245–6) was dissolved in NaOH 1.0N in aqueous solution (VWR BDH7222); and the rhodamine B (Alfa Aesar A13572) was dissolved in water. The fluorophore mixtures were acquired by mixing the fluorescein and rhodamine B lifetime standards described above with different mole ratios.

3. Results

3.1 Instant FLIM system and principle

Built upon on our preliminary work presented in Ref. [46], instant FLIM uses a radio frequency (RF) analog signal processing approach, where the two-photon excitation fluorescence (2PEF) signal is split to four ways and mixed with the phase-shifted 80 MHz reference signals from the Ti:sapphire laser in a multiplexing manner (Fig. 1A; see Fig. S1 and Fig. S2 for details). It is essentially a homodyne FD-FLIM method to extract the lifetime information from the first harmonic of the 80 MHz laser repetition in fluorescence. We employed the reference signal from the laser because the laser repetition rate had a ±1 MHz variance so a fixed-frequency external reference signal could introduce errors, and the implementation was cost-effective. In instant FLIM, the four paths of the fluorescence and reference signals are operated independently and simultaneously during each measurement, and the mixers' outputs are DC signals that can be digitized by almost any data acquisition devices. The parallel, analog signal processing enabled simultaneous acquisition and instantaneous processing of 2PEF intensity and lifetime images and phasor plots for single- or multi-exponential decay analysis (Fig. 1B; see Section S1 and Section S2 for details). Consequently, no additional acquisition time compared to conventional two-photon intensity measurement was required in instant FLIM, and it was deconvolution-free and fit-free, as lifetime images and phasor plots can be generated instantaneously through basic matrix operations with no extra computation time or memory, eliminating the bottleneck of state-of-the-art FLIM systems [15,16].

Fluorescence lifetime images alone are usually not enough to resolve the heterogeneity of fluorophores with multi-exponential decays, as different fluorophore compositions could result in the same lifetime measurements. Phasor plots, on the other hand, can resolve the fluorophore heterogeneity because different fluorophore compositions can alter the phasor components (horizontal coordinates g and vertical coordinates s) even if the average lifetime might be unaltered [35,36]. While phasor coordinates can be computed from any time-domain FLIM data using fast Fourier transforms, which are less computation- and time-consuming than curve-fitting, Laguerre expansion, and principal component analysis techniques [47–49], it is still difficult to generate phasor results immediately using a regular computer due to the GB/s data rates acquired with a state-of-the-art TD-FLIM system. On the contrary, instant FLIM generates phasor results immediately through basic matrix operations applied to the analog data acquired at MB/s rates. To confirm the accuracy of phasor measurements of the instant FLIM system, we acquired the phasor plots of four fluorophores with single-exponential decays, which are usually used as fluorescence lifetime standards as their lifetime values are stable and well-studied [44,45,50]. As shown in Fig. 1C, the phasors of these single-exponential fluorophores all located on the universal semicircle, and their lifetime measurements matched the expected values: coumarin 6 in methanol, 2.29 ± 0.05 ns; coumarin 6 in ethanol, 2.44 ± 0.05 ns; fluorescein, 3.96 ± 0.24 ns; and rhodamine B, 1.66 ± 0.02 ns. We then used the instant FLIM system to acquire the intensity and lifetime images and phasor plots of heterogeneous fluorophore mixtures consisting of fluorescein and rhodamine B: whereas the lifetimes of the mixtures of different mole ratios of fluorescein and rhodamine B, e.g., 15:1 and 7.5:1, were hard to distinguish

(Fig. 1D), their difference in the phasor plot (Fig. 1E) was evident and could be used to differentiate the two mixtures.

We next analyzed the SNR performance in lifetime measurements of an instant FLIM system and compared it with conventional FD-FLIM techniques (see Section S3 for details). The SNR performance was quantified using the *F*-value, i.e., photon economy, a widely used figure of merit independent of common factors such as fluorophore concentration and quantum efficiency to describe the sensitivity of FLIM techniques [10,51]. The *F*-value is defined as the ratio of the uncertainties in lifetime and intensity measurements: a smaller *F*-value is desired as it represents a more accurate lifetime measurement with better SNR performance; there is, however, a lower limit of 1 on an *F*-value, which only exists in an ideal shot-noise-limited FLIM system where the available photons are utilized as efficiently as physically possible. Through Monte Carlo simulations and analytical error-propagation analyses, we showed that instant FLIM has a lower *F*-value, and therefore superior SNR performance, when compared to conventional FD-FLIM techniques for all fluorophores with a lifetime shorter than 4.5 ns. Although the SNR performance of instant FLIM is not as good as that of TCSPC, which records almost all the photons in the fluorescence decay and has a nearly perfect *F*-value of 1 regardless of fluorescence lifetime values, the *F*-value of instant FLIM can approach 1 at certain lifetime values, which cannot be achieved using conventional FD-FLIM techniques. The superior SNR performance of instant FLIM was mainly achieved by efficiently utilizing the intrinsic 80 MHz mode-locked femtosecond laser pulses as the modulation source and employing the low-power external RF mixing, instead of the detector gain modulation used in conventional FD-FLIM systems [10,14].

With the simultaneous image acquisition, instantaneous data processing, and superior SNR performance, in this work, we demonstrated acquisition and processing of 2PEF intensity, lifetime, and phasor imaging data altogether in 12 μs/pixel using a pair of galvo scanners (Table S1). The 12 μs/pixel acquisition time in our instant FLIM system was mainly limited by the bandwidth (175 Hz for saw tooth waves) of our galvo scanners (Thorlabs GVS002), while the data processing time was around 2 ns/pixel running on an Intel Core i7–8750H 2.20 GHz laptop PC, which was orders of magnitude shorter than the image acquisition time. The pixel dwell time could be reduced to below 1 μs if resonant scanning mirrors or polygon scanners were used [16], where the intensity of the excitation laser beam needed to be increased accordingly to compensate for the signal loss. We used galvo scanners, instead of resonant mirrors or polygon scanners, mainly because galvo scanners are the most widely used scanners in conventional two-photon laser scanning microscopes. Nevertheless, thanks to the modular design of the cost-effective hardware (Fig. S1) and our open-source software (*Instant-FLIM-Control* and *Instant-FLIM-Analysis*) (Fig. S5), modifications to an instant FLIM system such as replacing the galvo scanners with resonant mirrors or polygon scanners can be easily implemented.

3.2 Instant FLIM with improved functionality, depth, and resolution

To make instant FLIM a comprehensive and high-performance platform for 4D *in vivo* lifetime imaging in deep brains and to present the full potential of instant FLIM, we improved its imaging functionality, depth, and resolution using phasor-based image

segmentation, adaptive optics (AO), and super-resolution FLIM techniques, respectively. These techniques lay the foundation of the biological results we present in the later sections. Note that while these techniques are not specific to instant FLIM and can be done on TD-FLIM, it is still difficult for many researchers to use these techniques in practice. Here, we present all the hardware and software implementation details of these techniques in this work and our open-source software packages, which become essential parts of the open-access toolkit of instant FLIM.

Phasor-based image segmentation techniques utilized phasor plots to segment pixels with similar phasor components (g and s) in a raw image to resolve fluorescence heterogeneity [3,36], thus improving the functionality of instant FLIM as an imaging tool. Here, we demonstrated two complementary approaches to implement phasor-based image segmentation: the manual phasor labeling [36] and the automatic phasor clustering techniques [37] (Fig. S6, A and B). In the phasor labeling approach, regions of interest (ROIs) were manually drawn on the phasor plot and the corresponding pixels in the raw image were labeled with different colors [36]. Fig. 2A shows an example of how different cellular structures in a 3D instant FLIM stack of a fixed Cx3cr1-GFP/+ mouse brain could be segmented into different pseudo-colored groups by manually labeling their phasors with ROIs on the phasor plot in Fig. 2B (Movie S1). On the other hand, the phasor clustering approach segmented an instant FLIM image by applying an unsupervised machine learning approach, i.e., K-means clustering, to automatically cluster the phasors into a specified number of groups (e.g., K=3 as shown in Fig. S6B) and labeling the corresponding pixels in the raw image with different colors [37]. The two segmentation methods are complementary: the phasor labeling approach is flexible but could lead to biased results, while the phasor clustering approach is unbiased and yet choosing a proper K value might require multiple trials.

We also added a sensorless AO setup as an optional module to our instant FLIM system (Fig. S1) to improve the penetration depth of our imaging system, which could be used to compensate for the optical aberrations in *in vivo* through-skull imaging deep in mouse brains [38]. We used one of three optimization algorithms (see Section S4 for details) to iteratively adjust the parameters of the wavefront shaping element, i.e., a deformable mirror in our setup, to improve the image quality quantified by an optimization metric [52,53]. We acquired a 3D lifetime stack of the brain, through-skull, in a living Cx3cr1-GFP/+ mouse using the instant FLIM system combined with the AO setup, and compared it with the 3D lifetime stack acquired from the same mouse but without AO (Movie S2). As shown in Fig. 2C, when there was no AO, our instant FLIM system could only achieve a penetration depth of 130 μm for through-skull 3D lifetime imaging in a living mouse brain; in comparison, by adding a well-optimized AO module into our instant FLIM system, the penetration depth for through-skull 3D FLIM in the same mouse was 300 μm, which was more than twice deeper than the depth without AO.

To present the full potential of instant FLIM, we further demonstrated super-resolution FLIM with our instant FLIM system using generalized stepwise optical saturation (GSOS) microscopy [41], which used two instant FLIM images acquired at different excitation powers to generate a super-resolution lifetime image with preserved lifetime information and

a $\sqrt{2}$-fold increase in both lateral and axial resolutions (see Section S5 for details). As shown in Fig. 2D, after linear combining two diffraction-limited (DL) lifetime images acquired with excitation powers of 8.95 mW and 10.61 mW, respectively, a super-resolution GSOS lifetime image with improved lateral resolution of the same field-of-view can be generated. Whereas we have utilized GSOS to generate 2D super-resolution FLIM images of fixed cells like the ones in Fig. 2D [41], we could not demonstrate GSOS in 3D due to the excessive time required to generate multiple 3D FLIM stacks under different excitation powers using conventional FLIM systems. In instant FLIM, however, due to the analog signal processing, 3D FLIM stacks could be generated at the same speed as 3D intensity stacks. Therefore, by using GSOS in an instant FLIM system, generating a 3D super-resolution FLIM stack only took twice the time of acquiring a 3D two-photon intensity stack. In Fig. S8, we generated a 3D super-resolution FLIM stack by applying GSOS to a pair of DL instant FLIM stacks of a fixed Cx3cr1-GFP/+ mouse brain acquired with excitation powers of 12.31 mW and 13.44 mW, respectively. As shown in Movie S3 and Fig. S8D, the cellular structures in the GSOS stack were better resolved with higher lateral (Fig. S8D, right) and axial resolutions (Fig. S8D, left) compared to the ones in the DL stacks.

3.3 In vivo 4D instant FLIM imaging in intact zebrafish and mouse brains

We characterized the *in vivo* performance of instant FLIM by measuring the fluorescence lifetime and phasor components of green fluorescence protein (GFP) expressed in microglia in living zebrafish and mouse brains, as microglia are critical for the functionality of the brain in homeostatic and disease states [54,55]. The GFP lifetime and the corresponding phasor coordinates are dependent on microenvironmental factors such as temperature [56], pH [2], and refractive index [57,58], and as cellular conditions and stress changes these chemical and physical properties, a change is seen in the GFP lifetime and phasor [59,60]. Before measuring GFP lifetimes *in vivo*, we performed an *in vitro* instant FLIM experiment by imaging GFP expressed in living MDA-MB-231-GFP cells under 18 different temperatures from 18.1 °C to 46.7 °C (Fig. S6C). Whereas the intensity images showed no clear distinctions under different temperatures, the fluorescence lifetimes decreased monotonically as temperature increased, which was likely caused by the increase in the rate constant of nonradiative processes as discussed in Ref. [2] and reported in Ref. [56]. We also used the phasor labeling (Fig. S6D) and phasor clustering (Fig. S6E) techniques to segment the images and demonstrated that the GFP phasors under different temperatures located differently on the phasor plot. The results confirmed that instant FLIM was able to detect changes in the intracellular microenvironment through lifetime and phasor measurements.

To test instant FLIM as an *in vivo* lifetime imaging modality, we first imaged *Tg(pu1:gfp)* zebrafish at 4 days post fertilization (dpf) using regulatory sequences of *pu1* to express GFP in myeloid cells including microglia and macrophages (Fig. 3A). So far, other than anatomical locations, identifiable markers that distinctly label these cells are limited. To determine if we could detect differences in GFP lifetimes within these cells, we imaged neural regions where both central nervous system (CNS) and peripheral nervous system (PNS) located myeloid cells could be detected and identifiable by their anatomical locations. The instant FLIM measurement reported at least two distinct GFP lifetime profiles using the phasor approach (Fig. 3, B-D). The phasors of PNS-located myeloid cells clustered

distinctly compared to that of CNS-located myeloid cells, which also segregated into at least two distinct clusters by their g component, suggesting that lifetime could report heterogeneity among myeloid cells. To investigate if lifetime differences were presented in distinct subdomains of individual CNS-located myeloid cells over time, we performed 4D instant FLIM by collecting 3D stacks every 15 minutes for 12 hours (Fig. 3, E and F). The 4D lifetime images in Fig. 3F show that the lifetimes of individual cellular subdomains changed over time as the cells migrated (white arrowheads denote subdomains with increased lifetimes over time). Note that the lifetime changes observed here are consistent with the GFP lifetime variations over the cell cycle as reported in Refs. [61,62]. However, these changes largely occurred within the cellular subdomains, whereas the average lifetimes of the cells remained stable during homeostasis (Fig. 3E).

We repeated this analysis using skull-thinned Cx3cr1-GFP/+ adult mice whose microglia were labeled with GFP (Fig. 4A). We also retro-orbitally injected Texas Red-Dextran into the animal to distinguish blood vessels from microglia. These adult microglia displayed dynamic and complex branching emanating from the cell body (Fig. 4B). Given that microglia in larval zebrafish displayed distinct lifetime subdomains, we hypothesized that adult microglia could also have distinct lifetimes in their cell bodies and surveilling protrusions. To test this, we measured τ, g, and s and compared these values between the cell bodies and protrusions. While we did not detect differences in g and s, the surveilling protrusions displayed increased τ compared to that of the cell bodies (Fig. 4, C and D), indicating that the protrusions had distinct changes in their microenvironment while interacting with other neural cell types. We also employed 4D instant FLIM by taking 3D stacks of the mouse microglia every two minutes for six minutes (Fig. 4, E and F). These images demonstrated that while the microglia had dynamic processes, under homeostatic conditions, the lifetimes of the cell bodies and surveilling protrusions were stable.

3.4 In vivo 4D instant FLIM imaging in injured zebrafish and mouse brains

As the brain's immune cells, microglia sense injury by continuously surveying the parenchyma with highly motile processes and converging to the site of injury to establish a barrier between the healthy and injured brain tissue [55,63]. We next used instant FLIM to determine if we could detect lifetime changes in microglia when they responded to brain injury. To do this, we created lesions in the larval *Tg(pu1:gfp)* zebrafish brain with the femtosecond laser and acquired 4D instant FLIM movies of microglial response to the site of injury by collecting 3D stacks every 15 minutes for 12 hours (Fig. 5A). Consistent with the injury response [63], microglia migrated to the site of injury (Fig. 5B; Movie S4). We investigated the phasors extracted from the 4D instant FLIM measurement. As shown in Fig. 5C, the phasors of pre-injury microglia clustered together; from 0 to 60 minutes post-injury (mpi), the phasors segregated into two clusters in opposite directions; this clustering continued after 60 mpi with few phasors resembling pre-injury ones. Meanwhile, in plotting average τ, g, and s values, we detected decreased s components in microglia after injury (Fig. 5D). We next analyzed the lifetimes of whole microglia and their individual cellular subdomains in response to injury (Fig. 5, E and F). After injury, both the microglia and subdomains adjusted their lifetimes, as denoted by the change in average lifetime values (Fig. 5E) and the increase of the number of red subdomains (red denoting longer lifetimes)

(Fig. 5F), with continuing changes through 75 mpi. These observations demonstrated instant FLIM's capacity to detect lifetime changes *in vivo* after physiological challenges such as laser injury.

We then used instant FLIM to investigate if similar lifetime changes could be detected in adult mouse microglia when they responded to brain injury. We created lesions in the skull-thinned Cx3cr1-GFP/+ mouse brain with the femtosecond laser and acquired 4D instant FLIM movies of microglial dynamics in response to injury by collecting 3D stacks every two minutes for an hour (Fig. 6A). Adult mouse microglia were markedly more abundant than larval zebrafish microglia. Consistent with the observations reported in Ref. [63], the laser injury in the adult mouse brain parenchyma induced an instantaneous response from the microglia where processes were extended toward the site of injury (Fig. 6B; Movie S5). This was in contrast with microglia in larval zebrafish which utilized whole-cell migrations to the site of injury. Adult mouse microglial processes surrounded the lesion site similar to the cloaking arrangement of macrophages in the PNS [64]. We first compared lifetime changes from before the injury (−2 mpi) to after the microglia have extended their processes to the injury site (22 mpi) (Fig. 6C). To do this, we measured the lifetimes and phasor components of the cell bodies, responding protrusions, and protrusion tips which were migrating to the site of injury (Fig. 6D). These measurements did not detect changes in τ, g, or s from −2 mpi to 22 mpi but did detect differences in τ and g between each of the cellular subdomains. These data suggested that adult microglia maintained subcellular lifetime and phasor differences while responding to injury (Movie S6). Further, we analyzed lifetime dynamics throughout the process of protrusion extension to cloak the injury site (Fig. 6, E and F). These measurements indicated that lifetimes and phasors in each subdomain of the microglia remained relatively stable during early extension and cloaking of the injury site (Fig. 6E). Considering the stability of lifetime and phasor information of adult mouse microglia in response to injury, we used both the phasor labeling and phasor clustering approaches to segment the 4D instant FLIM voxels into different cellular structures (e.g., cell bodies, protrusions, protrusion tips, etc.) based on the similarity of their phasors and distinguished their responses to the laser injury (Movie S7).

Taken together, these results demonstrate the capability of instant FLIM to delineate the dynamics of lifetimes and phasors in diverse cellular subdomains in zebrafish and mouse brains *in vivo*. They also highlight an important contrast in microglial responses to injury early in development and adulthood: microglia in larval zebrafish demonstrated lifetime changes after injury, while this effect was not observed in microglia in adult mice. Whereas the fundamental causes of the GFP lifetime or phasor variations in microglial subdomains are beyond the scope of this article, these variations measured by instant FLIM will be beneficial to distinguish and label cellular subdomains in microglia and understand their roles in the immune surveillance process [55].

4. Discussion

Through analog signal processing, we have demonstrated instant FLIM as a novel FD-FLIM system that enables simultaneous acquisition and instantaneous processing of 2PEF intensity, lifetime, and phasor imaging data. However, the performance does not come

without caveats. First, since instant FLIM utilizes the intrinsic femtosecond laser pulses as the modulation source, the modulation frequency is fixed at 80 MHz; therefore, as shown in Fig. S4C, the SNR performance in lifetime measurements, quantified by the *F*-value, will become worse for fluorophores with longer lifetimes. As a result, instant FLIM will perform best with short-lifetime fluorophores such as rhodamine B and indocyanine green (ICG) [65]; for long-lifetime fluorophores or samples consisting of a wide range of lifetime components [66], the pixel dwell time for instant FLIM measurements should be increased accordingly to compensate for the lower photon economy. Second, while it is advantageous for instant FLIM to generate lifetime images and phasor plots directly without recording fluorescence decay curves to eliminate limitations in computer memory and bandwidth, users who are familiar with TD-FLIM systems may find it less intuitive or not straightforward to interpret the lifetime results. This is a trade-off between functionality and cost, as fluorescence decay curves can only be fully recorded using expensive TCSPC or high-frequency digitizers. Third, due to the electronic and RF components required to implement the analog signal processing in instant FLIM, additional electronic noise such as thermal noise and electromagnetic interference from the environment could be introduced to the lifetime measurement if the instruments were not well connected or shielded. In our experience, however, using low-noise amplifiers and properly shielding the electronics could successfully suppress the additional noise, and shot-noise limited measurements could be achieved.

The four-phase analog signal processing in the current instant FLIM system can be further improved. Theoretically, to extract lifetime information via homodyne FD-FLIM measurements, minimally only three phase images are required, and the lifetime measurement accuracy can be further improved if more phase images, e.g., 12, are employed [27]. In conventional FD-FLIM systems, these phase images need to be captured sequentially, so acquiring more phase images requires a longer acquisition time. Meanwhile, for more phase images, the processing for lifetime information becomes more complicated and time-consuming, as complex trigonometry calculations or curve fittings are required. In this work, we only acquired four phase images to reduce the cost of the system and the complexity of lifetime and phasor calculations. Nevertheless, following the principle of multiplexing analog signal processing, the current instant FLIM setup could be readily expanded to allow simultaneous acquisition of 12 or more phase images, where the 2PEF signal could be split to 12 or more paths and mixed with the phase-shifted reference signals from the femtosecond laser; therefore, the lifetime measurement accuracy of instant FLIM could be improved while no extra image acquisition time would be needed.

In conclusion, we have presented instant FLIM as a powerful tool for high-speed, long-term, 4D *in vivo* FLIM that allows real-time streaming of 2PEF intensity, lifetime, and phasor imaging data. As shown in Table S3, compared to existing FLIM techniques, the novel and unique aspects of instant FLIM include (1) the instantaneous data processing that allows real-time streaming of lifetime results, (2) the significantly reduced requirement for computer memory and bandwidth, and (3) the high-performance in imaging speed, penetration depth, and resolution that enables the deepest and longest *in vivo* FLIM measurements to date. We have also demonstrated that an instant FLIM system could be combined with phasor labeling and clustering, AO, and GSOS to provide versatile

phasor-based image segmentation, deep penetration depths, and super-resolution FLIM performances. The benefits of instant FLIM have been demonstrated extensively through the 4D *in vivo* FLIM experiments of intact and injured mouse and zebrafish brains. Using instant FLIM, we have achieved unprecedented *in vivo* FLIM imaging depth (300 μm through skull) and duration (12 hours non-stop) and identified cellular subdomains in microglia, which will be beneficial for biologists to understand their roles in the immune surveillance process. Biologically, the identification of cellular subdomains with different fluorescence lifetime properties of a cytosolic fluorophore was surprising. These domains could be the result of a variety of phenomena such as distinct cell signaling hubs or organelle density. Regardless, these results were accomplished by upgrading a conventional two-photon laser scanning microscope using cost-effective off-the-shelf components with a total cost less than $2,500 and our fully open-source, highly modularized, and user-friendly software packages (*Instant-FLIM-Control* and *Instant-FLIM-Analysis*). As a result, instant FLIM can be easily accessed by many labs and has the potential to enable future discoveries in biology, including the mechanism of lifetime subdomains identified here, in addition to a wide variety of disciplines.

Supplementary Material

Refer to Web version on PubMed Central for supplementary material.

Acknowledgments.

We thank V. Mannam, X. Yuan, and O. Abdalsalam for discussion. We also thank L. Li for proofreading this manuscript.

Funding.

This work was supported by the University of Notre Dame, the Center for Zebrafish Research and Center of Stem Cells and Regenerative Medicine at the University of Notre Dame, the National Science Foundation under Grant No. CBET-1554516 (S.S.H.), the National Institutes of Health R01 CA194697, R01 CA222405 (S.Z.), R01 NS107553 (C.J.S), the Elizabeth and Michael Gallagher Family (C.J.S.), the Alfred P. Sloan Foundation (C.J.S.), and the Berry Family Foundation Graduate Fellowship of Advanced Diagnostics & Therapeutics (AD&T) (Y.Z.).

Data availability.

The repositories of the open-source *Instant-FLIM-Control* (https://github.com/yzhang34/Instant-FLIM-Control.git) and *Instant-FLIM-Analysis* (https://github.com/yzhang34/Instant-FLIM-Analysis.git) software are hosted on GitHub and they are freely available for academic use. Detailed protocols describing how to use the two software packages are included within the repositories. All data needed to evaluate the conclusions in this paper are present in the paper and/or the Supplementary Materials. Additional data related to this paper may be requested from the authors.

References

1. Lichtman JW and Conchello J-A, “Fluorescence microscopy,” Nat. Methods 2, 910–919 (2005). [PubMed: 16299476]
2. Berezin MY and Achilefu S, “Fluorescence Lifetime Measurements and Biological Imaging,” Chem. Rev. 110, 2641–2684 (2010). [PubMed: 20356094]

3. Sun Y, Day RN, and Periasamy A, "Investigating protein-protein interactions in living cells using fluorescence lifetime imaging microscopy," Nat. Protoc. 6, 1324–1340 (2011). [PubMed: 21886099]
4. König K, "Review: Clinical in vivo multiphoton FLIM tomography," Methods Appl. Fluoresc. 8, 034002 (2020). [PubMed: 32320386]
5. Datta R, Heaster TM, Sharick JT, Gillette AA, and Skala MC, "Fluorescence lifetime imaging microscopy: fundamentals and advances in instrumentation, analysis, and applications," J. Biomed. Opt. 25, 1 (2020).
6. Denk W, Strickler JH, and Webb WW, "Two-photon laser scanning fluorescence microscopy.," Science 248, 73–6 (1990). [PubMed: 2321027]
7. Zipfel WR, Williams RM, and Webb WW, "Nonlinear magic: multiphoton microscopy in the biosciences," Nat. Biotechnol. 21, 1369–1377 (2003). [PubMed: 14595365]
8. Sakadžić S, Roussakis E, a Yaseen M, Mandeville ET, Srinivasan VJ, Arai K, Ruvinskaya S, Devor A, Lo EH, a Vinogradov S, and a Boas D, "Two-photon high-resolution measurement of partial pressure of oxygen in cerebral vasculature and tissue," Nat. Methods 7, 755–759 (2010). [PubMed: 20693997]
9. Howard SS, Straub A, Horton NG, Kobat D, and Xu C, "Frequency-multiplexed in vivo multiphoton phosphorescence lifetime microscopy," Nat. Photonics 7, 33–37 (2012). [PubMed: 23472061]
10. Philip J and Carlsson K, "Theoretical investigation of the signal-to-noise ratio in fluorescence lifetime imaging," J. Opt. Soc. Am. A 20, 368–379 (2003).
11. Booth MJ and Wilson T, "Low-cost, frequency-domain, fluorescence lifetime confocal microscopy," J. Microsc. 214, 36–42 (2004). [PubMed: 15049866]
12. Wouters FS, "The physics and biology of fluorescence microscopy in the life sciences," Contemp. Phys. 47, 239–255 (2006).
13. Colyer RA, Lee C, and Gratton E, "A novel fluorescence lifetime imaging system that optimizes photon efficiency," Microsc. Res. Tech. 71, 201–213 (2008). [PubMed: 18008362]
14. Zhang Y, Khan AA, Vigil GD, and Howard SS, "Investigation of signal-to-noise ratio in frequency-domain multiphoton fluorescence lifetime imaging microscopy," J. Opt. Soc. Am. A 33, B1 (2016).
15. Ryu J, Kang U, Kim J, Kim H, Kang JH, Kim H, Sohn DK, Jeong J, Yoo H, and Gweon B, "Real-time visualization of two-photon fluorescence lifetime imaging microscopy using a wavelength-tunable femtosecond pulsed laser," Biomed. Opt. Express 9, 3449 (2018). [PubMed: 29984109]
16. Bower AJ, Li J, Chaney EJ, Marjanovic M, Spillman DR, and Boppart SA, "High-speed imaging of transient metabolic dynamics using two-photon fluorescence lifetime imaging microscopy," Optica 5, 1290 (2018). [PubMed: 30984802]
17. Ameer-Beg S, Suhling K, and Kuimova M, "Special issue on fluorescence lifetime imaging (FLIM): from fundamentals to applications," Methods Appl. Fluoresc. 8, 040401 (2020). [PubMed: 33021203]
18. Becker W, Bergmann A, Hink MA, König K, Benndorf K, and Biskup C, "Fluorescence lifetime imaging by time-correlated single-photon counting," Microsc. Res. Tech. 63, 58–66 (2004). [PubMed: 14677134]
19. Skala MC, Riching KM, Bird DK, Gendron-Fitzpatrick A, Eickhoff J, Eliceiri KW, Keely PJ, and Ramanujam N, "In vivo multiphoton fluorescence lifetime imaging of protein-bound and free nicotinamide adenine dinucleotide in normal and precancerous epithelia," J. Biomed. Opt. 12, 024014 (2007). [PubMed: 17477729]
20. Rinnenthal JL, Börnchen C, Radbruch H, Andresen V, Mossakowski A, Siffrin V, Seelemann T, Spiecker H, Moll I, Herz J, Hauser AE, Zipp F, Behne MJ, and Niesner R, "Parallelized TCSPC for Dynamic Intravital Fluorescence Lifetime Imaging: Quantifying Neuronal Dysfunction in Neuroinflammation," PLoS One 8, e60100 (2013). [PubMed: 23613717]
21. Poland SP, Krstajić N, Monypenny J, Coelho S, Tyndall D, Walker RJ, Devauges V, Richardson J, Dutton N, Barber P, Li DD-U, Suhling K, Ng T, Henderson RK, and Ameer-Beg SM, "A high speed multifocal multiphoton fluorescence lifetime imaging microscope for live-cell FRET imaging," Biomed. Opt. Express 6, 277 (2015). [PubMed: 25780724]

22. Yaseen MA, Sutin J, Wu W, Fu B, Uhlirova H, Devor A, Boas DA, and Sakadžić S, "Fluorescence lifetime microscopy of NADH distinguishes alterations in cerebral metabolism in vivo," Biomed. Opt. Express 8, 2368 (2017). [PubMed: 28663879]
23. Levitt JA, Poland SP, Krstajic N, Pfisterer K, Erdogan A, Barber PR, Parsons M, Henderson RK, and Ameer-Beg SM, "Quantitative real-time imaging of intracellular FRET biosensor dynamics using rapid multi-beam confocal FLIM," Sci. Rep. 10, 5146 (2020). [PubMed: 32198437]
24. So PTC, French T, Yu WM, Berland KM, and Dong CY, "Time-resolved fluorescence microscopy using two-photon excitation," Bioimaging 3, 49–63 (1995).
25. Schneider PC and Clegg RM, "Rapid acquisition, analysis, and display of fluorescence lifetime-resolved images for real-time applications," Rev. Sci. Instrum. 68, 4107–4119 (1997).
26. Gratton E, "Fluorescence lifetime imaging for the two-photon microscope: time-domain and frequency-domain methods," J. Biomed. Opt. 8, 381 (2003). [PubMed: 12880343]
27. Raspe M, Kedziora KM, van den Broek B, Zhao Q, de Jong S, Herz J, Mastop M, Goedhart J, Gadella TWJ, Young IT, and Jalink K, "siFLIM: single-image frequency-domain FLIM provides fast and photon-efficient lifetime data," Nat. Methods 13, 501–504 (2016). [PubMed: 27088314]
28. Becker W, The Bh TCSPC Handbook (2014).
29. Li D-U, Walker R, Richardson J, Rae B, Buts A, Renshaw D, and Henderson R, "Hardware implementation and calibration of background noise for an integration-based fluorescence lifetime sensing algorithm," J. Opt. Soc. Am. A 26, 804 (2009).
30. Li D-U, "Hardware implementation algorithm and error analysis of high-speed fluorescence lifetime sensing systems using center-of-mass method," J. Biomed. Opt. 15, 017006 (2010). [PubMed: 20210480]
31. Poland SP, Erdogan AT, Krstajić N, Levitt J, Devauges V, Walker RJ, Li DD-U, Ameer-Beg SM, and Henderson RK, "New high-speed centre of mass method incorporating background subtraction for accurate determination of fluorescence lifetime," Opt. Express 24, 6899 (2016). [PubMed: 27136986]
32. Mitchell AC, Wall JE, Murray JG, and Morgan CG, "Direct modulation of the effective sensitivity of a CCD detector: a new approach to time-resolved fluorescence imaging," J. Microsc. 206, 225–232 (2002). [PubMed: 12067367]
33. Zhao Q, Schelen B, Schouten R, van den Oever R, Leenen R, van Kuijk H, Peters I, Polderdijk F, Bosiers J, Raspe M, Jalink K, de Jong JGS, van Geest B, Stoop K, and Young IT, "Modulated electron-multiplied fluorescence lifetime imaging microscope: all-solid-state camera for fluorescence lifetime imaging," J. Biomed. Opt. 17, 126020 (2012). [PubMed: 23323290]
34. Helmchen F and Denk W, "Deep tissue two-photon microscopy," Nat. Methods 2, 932–940 (2005). [PubMed: 16299478]
35. a Digman M, Caiolfa VR, Zamai M, and Gratton E, "The Phasor Approach to Fluorescence Lifetime Imaging Analysis," Biophys. J. 94, L14–L16 (2008). [PubMed: 17981902]
36. Ranjit S, Malacrida L, Jameson DM, and Gratton E, "Fit-free analysis of fluorescence lifetime imaging data using the phasor approach," Nat. Protoc. 13, 1979–2004 (2018). [PubMed: 30190551]
37. Zhang Y, Hato T, Dagher PC, Nichols EL, Smith CJ, Dunn KW, and Howard SS, "Automatic segmentation of intravital fluorescence microscopy images by K-means clustering of FLIM phasors," Opt. Lett. 44, 3928–3931 (2019). [PubMed: 31415514]
38. Ji N, "Adaptive optical fluorescence microscopy," Nat. Methods 14, 374–380 (2017). [PubMed: 28362438]
39. Lesoine MD, Bose S, Petrich JW, and Smith EA, "Supercontinuum Stimulated Emission Depletion Fluorescence Lifetime Imaging," J. Phys. Chem. B 116, 7821–7826 (2012). [PubMed: 22694181]
40. Marsh RJ, Culley S, and Bain AJ, "Low power super resolution fluorescence microscopy by lifetime modification and image reconstruction," Opt. Express 22, 12327 (2014). [PubMed: 24921351]
41. Zhang Y, Benirschke D, Abdalsalam O, and Howard SS, "Generalized stepwise optical saturation enables super-resolution fluorescence lifetime imaging microscopy," Biomed. Opt. Express 9, 4077 (2018). [PubMed: 30615706]

42. Parslow A, Cardona A, and Bryson-Richardson RJ, “Sample Drift Correction Following 4D Confocal Time-lapse Imaging,” J. Vis. Exp. 1–4 (2014).
43. Grutzendler J, Kasthuri N, and Gan W-B, “Long-term dendritic spine stability in the adult cortex,” Nature 420, 812–816 (2002). [PubMed: 12490949]
44. Boens N, Qin W, Basarić N, Hofkens J, Ameloot M, Pouget J, Lefèvre J-P, Valeur B, Gratton E, VandeVen M, Silva ND, Engelborghs Y, Willaert K, Sillen A, Rumbles G, Phillips D, Visser AJWG, van Hoek A, Lakowicz JR, Malak H, Gryczynski I, Szabo AG, Krajcarski DT, Tamai N, and Miura A, “Fluorescence Lifetime Standards for Time and Frequency Domain Fluorescence Spectroscopy,” Anal. Chem. 79, 2137–2149 (2007). [PubMed: 17269654]
45. Kristoffersen AS, Erga SR, Hamre B, and Frette Ø, “Testing Fluorescence Lifetime Standards using Two-Photon Excitation and Time-Domain Instrumentation: Rhodamine B, Coumarin 6 and Lucifer Yellow,” J. Fluoresc. 24, 1015–1024 (2014). [PubMed: 24866152]
46. Zhang Y, Guldner IH, Nichols EL, Benirschke D, Smith CJ, Zhang S, and Howard SS, “Three-dimensional deep tissue multiphoton frequency-domain fluorescence lifetime imaging microscopy via phase multiplexing and adaptive optics,” in Proc. SPIE 10882, Multiphoton Microscopy in the Biomedical Sciences XIX, Periasamy A, So PT, and König K, eds. (SPIE, 2019), p. 108822H.
47. Jo JA, Fang Q, Papaioannou T, and Marcu L, “Fast model-free deconvolution of fluorescence decay for analysis of biological systems,” J. Biomed. Opt. 9, 743 (2004). [PubMed: 15250761]
48. Jo JA, Fang Qiyin, and Marcu L, “Ultrafast method for the analysis of fluorescence lifetime imaging microscopy data based on the Laguerre expansion technique,” IEEE J. Sel. Top. Quantum Electron. 11, 835–845 (2005).
49. Le Marois A, Labouesse S, Suhling K, and Heintzmann R, “Noise-Corrected Principal Component Analysis of fluorescence lifetime imaging data,” J. Biophotonics 10, 1124–1133 (2017). [PubMed: 27943625]
50. Sjöback R, Nygren J, and Kubista M, “Absorption and fluorescence properties of fluorescein,” Spectrochim. Acta Part A Mol. Biomol. Spectrosc. 51, L7–L21 (1995).
51. Esposito A, Gerritsen HC, and Wouters FS, “Optimizing frequency-domain fluorescence lifetime sensing for high-throughput applications: photon economy and acquisition speed,” J. Opt. Soc. Am. A 24, 3261 (2007).
52. Debarre D, Booth MJ, and Wilson T, “Image based adaptive optics through optimisation of low spatial frequencies,” Opt. Express 15, 8176 (2007). [PubMed: 19547145]
53. Palczewska G, Dong Z, Golczak M, Hunter JJ, Williams DR, Alexander NS, and Palczewski K, “Noninvasive two-photon microscopy imaging of mouse retina and retinal pigment epithelium through the pupil of the eye,” Nat. Med. 20, 785–789 (2014). [PubMed: 24952647]
54. Peri F and Nüsslein-Volhard C, “Live Imaging of Neuronal Degradation by Microglia Reveals a Role for v0-ATPase a1 in Phagosomal Fusion In Vivo,” Cell 133, 916–927 (2008). [PubMed: 18510934]
55. Bernier L, Bohlen CJ, York EM, Stevens B, Barres BA, Macvicar BA, Bernier L, Bohlen CJ, York EM, Choi HB, and Kamyabi A, “Nanoscale Surveillance of the Brain by Microglia via Article Nanoscale Surveillance of the Brain by Microglia via cAMP-Regulated Filopodia,” Cell Rep. 27, 2895–2908.e4 (2019). [PubMed: 31167136]
56. Leiderman P, Huppert D, and Agmon N, “Transition in the temperature-dependence of GFP fluorescence: From proton wires to proton exit,” Biophys. J. 90, 1009–1018 (2006). [PubMed: 16284263]
57. Suhling K, Siegel J, Phillips D, French PMW, Lévêque-Fort S, Webb SED, and Davis DM, “Imaging the Environment of Green Fluorescent Protein,” Biophys. J. 83, 3589–3595 (2002). [PubMed: 12496126]
58. van Manen H-J, Verkuijlen P, Wittendorp P, Subramaniam V, van den Berg TK, Roos D, and Otto C, “Refractive Index Sensing of Green Fluorescent Proteins in Living Cells Using Fluorescence Lifetime Imaging Microscopy,” Biophys. J. 94, L67–L69 (2008). [PubMed: 18223002]
59. Nakabayashi T, Nagao I, Kinjo M, Aoki Y, Tanaka M, and Ohta N, “Stress-induced environmental changes in a single cell as revealed by fluorescence lifetime imaging,” Photochem. Photobiol. Sci. 7, 671 (2008). [PubMed: 18528550]

60. Ito T, Oshita S, Nakabayashi T, Sun F, Kinjo M, and Ohta N, “Fluorescence lifetime images of green fluorescent protein in HeLa cells during TNF-α induced apoptosis,” Photochem. Photobiol. Sci. 8, 763 (2009). [PubMed: 19492103]

61. Pliss A, Zhao L, Ohulchanskyy TY, Qu J, and Prasad PN, “Fluorescence Lifetime of Fluorescent Proteins as an Intracellular Environment Probe Sensing the Cell Cycle Progression,” ACS Chem. Biol. 7, 1385–1392 (2012). [PubMed: 22594453]

62. Pliss A and Prasad PN, “High resolution mapping of subcellular refractive index by Fluorescence Lifetime Imaging: a next frontier in quantitative cell science?,” Methods Appl. Fluoresc. 8, 032001 (2020). [PubMed: 32235079]

63. Davalos D, Grutzendler J, Yang G, Kim JV, Zuo Y, Jung S, Littman DR, Dustin ML, and Gan W-B, “ATP mediates rapid microglial response to local brain injury in vivo,” Nat. Neurosci. 8, 752–758 (2005). [PubMed: 15895084]

64. Uderhardt S, Martins AJ, Tsang JS, Lämmermann T, and Germain RN, “Resident Macrophages Cloak Tissue Microlesions to Prevent Neutrophil-Driven Inflammatory Damage,” Cell 177, 541–555.e17 (2019). [PubMed: 30955887]

65. Gerega A, Zolek N, Soltysinski T, Milej D, Sawosz P, Toczylowska B, and Liebert A, “Wavelength-resolved measurements of fluorescence lifetime of indocyanine green,” J. Biomed. Opt. 16, 067010 (2011). [PubMed: 21721831]

66. Grant DM, McGinty J, McGhee EJ, Bunney TD, Owen DM, Talbot CB, Zhang W, Kumar S, Munro I, Lanigan PM, Kennedy GT, Dunsby C, Magee AI, Courtney P, Katan M, Neil MAA, and French PMW, “High speed optically sectioned fluorescence lifetime imaging permits study of live cell signaling events,” Opt. Express 15, 15656 (2007). [PubMed: 19550853]

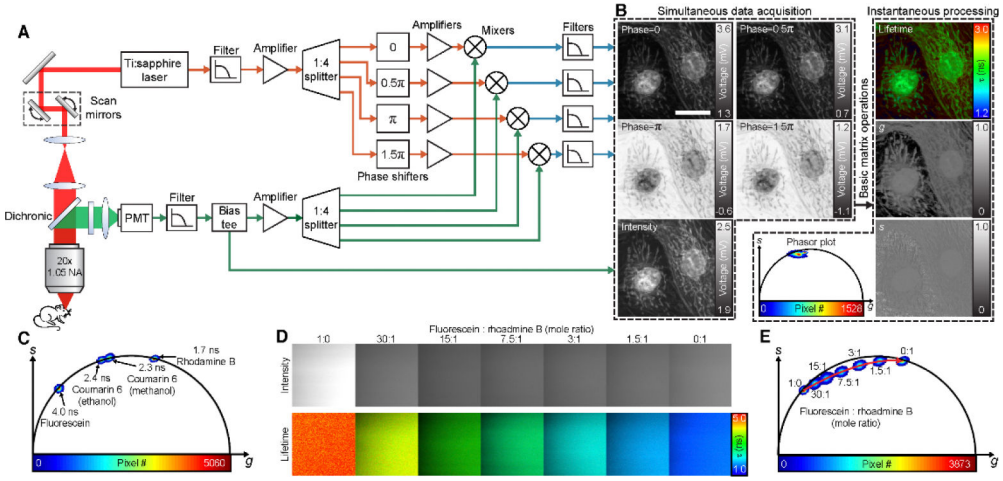

Fig. 1.

Instant FLIM system. (A) Brief diagram of an instant FLIM system. Excitation (red) is generated by a femtosecond laser and sent to a custom-built two-photon laser scanning microscope. Two-photon excitation fluorescence (green) is collected by a photomultiplier tube (PMT), whose signal is filtered and separated to two parts by a bias tee; the RF part is amplified, split to four ways, and mixed with the split laser reference signals with different phases introduced by four phase shifters; the filtered mixer signals and the bias tee's DC part are then simultaneously digitized by a data acquisition card. (B) Left, raw analog signals acquired simultaneously while imaging fixed BPAE cells. Right, lifetime, g, and s images and phasor plots generated instantaneously through basic matrix operations. (C) Phasor plot of four fluorescence lifetime standards in solution. (D) Intensity and lifetime images of fluorophore solutions mixed with different mole ratios of fluorescein and rhodamine B. (E) Phasor plot of the fluorophore mixtures in (D). The red arrow indicates how the phasors shift when more rhodamine B solution is added to the mixture. Scale bar, 20 μm.

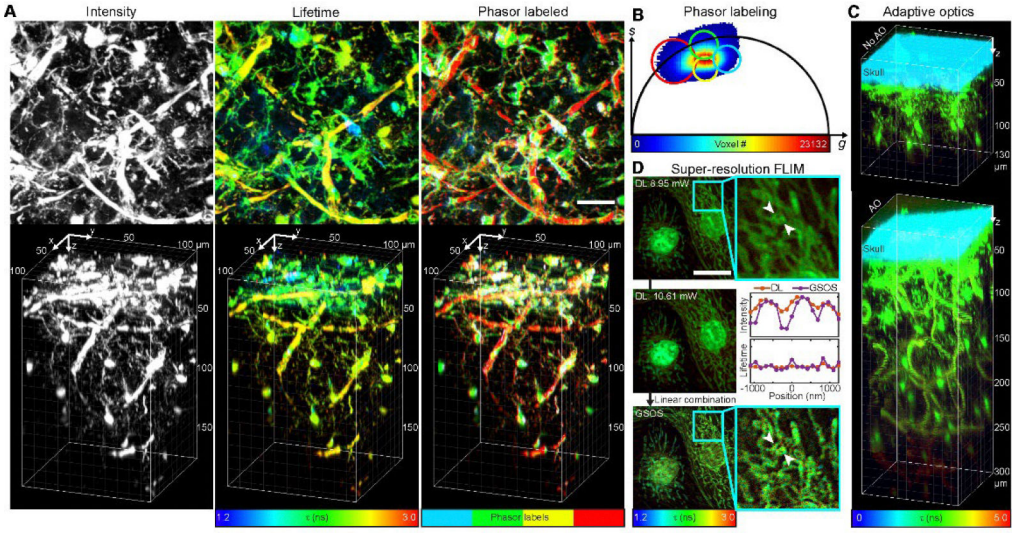

Fig. 2.

Instant FLIM with phasor labeling, adaptive optics, and super-resolution techniques. (A) Maximized z-projections (top) and 3D reconstructions (bottom) of the 2PEF intensity, lifetime, and phasor labeled stacks of a fixed Cx3cr1-GFP/+ mouse brain acquired simultaneously with an instant FLIM system. (B) Demonstration of the phasor labeling technique, where ROIs are drawn on the phasor plot of the fixed mouse brain to label different cellular structures in the phasor labeled stack in (A). (C) 3D reconstructed lifetime stacks of the intact brain in a living Cx3cr1-GFP/+ mouse acquired with an instant FLIM system without (top) and with (bottom) the adaptive optics (AO) technique. (D) Demonstration of super-resolution FLIM by applying the generalized stepwise optical saturation (GSOS) technique in an instant FLIM system, where the super-resolution GSOS lifetime image of fixed BPAE cells is obtained by linear combining two diffraction-limited (DL) instant FLIM images acquired with different excitation powers. Insets, magnified views. Middle, line profiles of the normalized intensity and lifetime values at the positions of the white arrowheads in the DL and GSOS images. Scale bars, 20 μm.

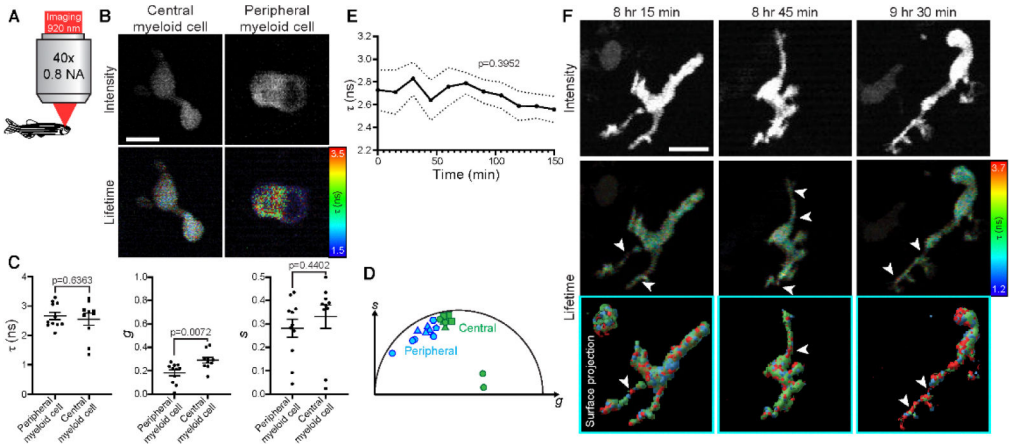

Fig. 3.

In vivo instant FLIM imaging in intact zebrafish brains. (A) Larval Tg(pu1:gfp) zebrafish at 4 dpf were imaged with a 920 nm laser using instant FLIM. (B) 2PEF intensity and lifetime maximized z-projection images of the CNS-located and PNS-located myeloid cells in the zebrafish. (C) Graphs of average lifetime (τ) and phasor (g and s) values in CNS-located (n=10 cells) and PNS-located (n=11 cells) myeloid cells. CNS-located cells have a larger g phasor component. (D) Plot representing the phasor locations of CNS-located (green) and PNS-located (blue) myeloid cells by their g and s phasor components. Each shape represents a measurement taken from different individual animals. (E) Average lifetime values of the zebrafish microglia over 150 minutes (n=8 cells). (F) 2PEF intensity and lifetime maximized z-projection images from a 12-hour 4D instant FLIM movie of the zebrafish microglia. Bottom, surface projections representing lifetime subdomains within the cell, where colors denote approximate lifetime values. White arrowheads denote cellular subdomains with increased lifetimes. Scale bars, 10 μm. (C) uses two-sided Student's t-tests. (E) uses one-way ANOVAs.

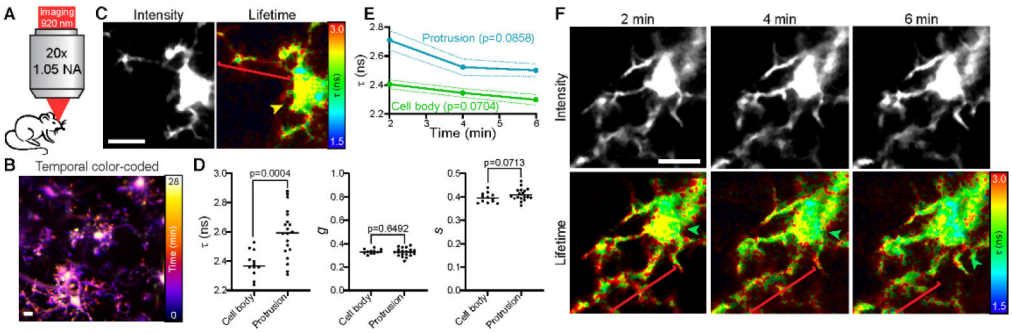

Fig. 4.

In vivo instant FLIM imaging in intact mouse brains. (A) Adult Cx3cr1-GFP/+ mice were imaged with a 920 nm laser using instant FLIM. (B) 2PEF intensity maximized z-projection image pseudo-colored to represent the temporal dynamics of the microglia. The temporal scale is shown on the right. (C) 2PEF intensity and lifetime maximized z-projection images of the mouse microglia. Bracket denotes the microglial protrusion, arrowhead denotes the cell body, and their colors represent approximate lifetime values. (D) Graphs of average lifetime (τ) and phasor (g and s) values in microglial cell bodies (n=12) and protrusions (n=20). (E) Average lifetime values of microglial cell bodies (green) and protrusions (blue) over 6 minutes (n=3 cells). (F) 2PEF intensity and lifetime maximized z-projection images from a 4D instant FLIM movie of the mouse microglia. Brackets denote microglial protrusions, arrowheads denote cell bodies, and their colors represent approximate lifetime values. Scale bars, 10 μm. (D) uses two-sided Student's t-tests. (E) uses one-way ANOVAs.

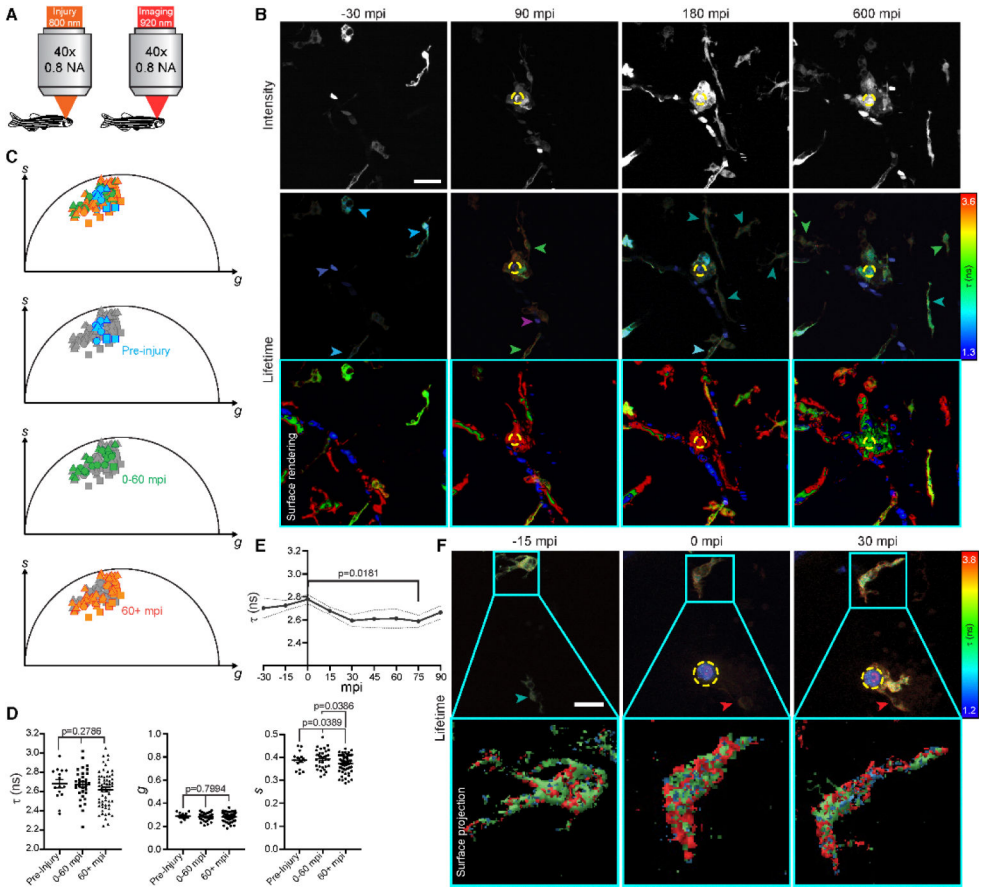

Fig. 5.

In vivo instant FLIM imaging in injured zebrafish brains. (A) Larval Tg(pu1:gfp) zebrafish at 4 dpf were imaged using instant FLIM following an injury induced by an 800 nm laser. (B) 2PEF intensity and lifetime maximized z-projection images from a 12-hour 4D instant FLIM movie in the zebrafish brain before and after laser injury. Mpi, minutes post-injury. Bottom, surface rendering of the lifetime images to better differentiate the cellular structures. Dashed yellow circle denotes the lesion site. Arrowheads denote approximate lifetime values. (C) Plot representing the phasor locations of microglia before injury (blue), 0–60 mpi (green), and 60+ mpi (orange). Each shape represents a measurement taken from different individual animals. (D) Graphs of average τ, g, and s values in microglia before injury (n=15 cells), 0–60 mpi (n=33 cells), and 60+ mpi (n=62 cells). (E) Average lifetime values of the microglia before and after injury (n=9 cells). (F) Lifetime maximized z-projection images from a 4-hour 4D instant FLIM movie of the microglia before and after injury. Insets, surface representation of changing lifetime subdomains within single microglia, where colors denote approximate lifetime values. Dashed yellow circle denotes the lesion site. Arrowheads denote approximate lifetime values. Scale bars, 10 μm. (D) and (E) use Tukey's HSD tests.

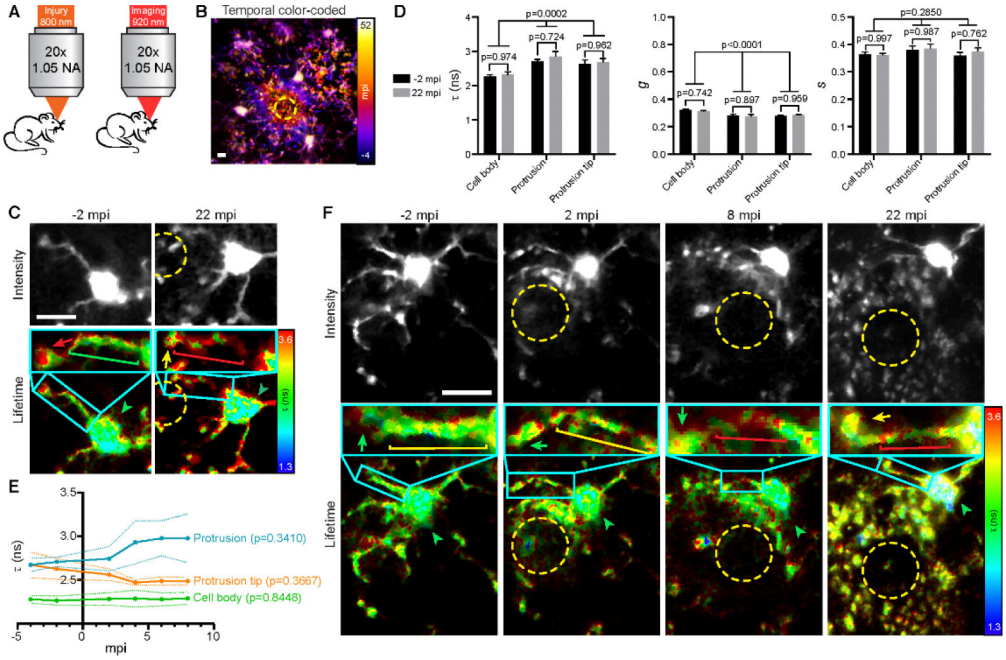

Fig. 6.

In vivo instant FLIM imaging in injured mouse brains. (A) Adult Cx3cr1-GFP/+ mice were imaged using instant FLIM following an injury induced by an 800 nm laser. (B) 2PEF intensity maximized z-projection image pseudo-colored to represent the temporal dynamics of the microglia in response to injury. The temporal scale is shown on the right. Dashed yellow circle denotes the lesion site. (C) Intensity and lifetime maximized z-projection images from a 4D instant FLIM movie in the mouse brain at −2 mpi and 22 mpi. Dashed yellow circle denotes the lesion site. Arrowheads denote cell bodies, brackets denote protrusions, and arrows denote protrusion tips. Colors denote approximate lifetime values. Insets show magnified views of the protrusions. (D) Graphs of average τ, g, and s values in cell bodies (n=5), protrusions (n=5), and protrusion tips (n=5) at −2 mpi and 22 mpi. (E) Average lifetime values of cell bodies, protrusions, and protrusion tips before and after injury (n=5 cells). (F) Intensity and lifetime maximized z-projection images from a 30-min 4D instant FLIM movie of the microglia before and after injury. Annotations are identical to the ones in (C). Scale bars, 10 μm. (D) uses two-way ANOVAs with multiple comparisons. (E) uses one-way ANOVAs.